ADVANCED MATERIALS INTERFACES
www.advmatinterfaces.de

Multidimensional Morphology Control for PS-b-P_4VP Templated Mesoporous Iron (III) Oxide Thin Films

*Shanshan Yin, Wei Cao, Qing Ji, Yajun Cheng, Lin Song, Nian Li, Christian L. Weindl, Matthias Schwartzkopf, Stephan V. Roth, and Peter Müller-Buschbaum**

Mesoporous α-Fe_2O_3 thin films with large area homogeneity demonstrate tremendous potential in multiple applications. In the present work, the synthesis of morphology-controlled α-Fe_2O_3 thin films is realized with polystyrene-block-poly(4-vinyl pyridine) (PS-b-P_4VP) diblock copolymer assisted sol-gel chemistry. The solvent category (DMF and 1,4-dioxane) and polymer-to-$FeCl_3$ ratio used for the solution preparation are systematically varied to tune the morphology of the thin films. For both solvents, DMF and 1,4-dioxane, nanocluster structures are obtained with low PS-b-P_4VP concentration. When the concentration of PS-b-P_4VP reaches the critical micelle concentration, spherical and wormlike porous structures are specifically formed in the DMF and 1,4-dioxane solvent system, respectively. Further increasing the polymer-to-$FeCl_3$ ratios leads to the enlargement of the spherical pore sizes in the DMF system, whereas the center-to-center distances of the wormlike structures in the 1,4-dioxane system decrease. Moreover, DMF/1,4-dioxane solvent mixtures with different volume ratios are applied for the sol–gel solution preparation to gain more insight into how the solvent selectivity affects the thin film morphology. By adjusting the preferential affinity of the solvent mixture to the polymer blocks, a spherical to wormlike pore shape transition is observed with a critical $\Delta\chi$ value of around 0.77.

1. Introduction

Hematite (α-Fe_2O_3), as the most common iron oxide polymorph, is characterized by its abundance, nontoxicity, good thermodynamic, and chemical stability as well as large bandgap (around 2.1 eV).[1–4] Compared with the bulk form, nanostructured α-Fe_2O_3 exhibits more size-dependent properties induced by the high surface area and quantum confinement.[5–8] Assembly of α-Fe_2O_3 nanoparticles (NPs) into periodic arrays has attracted high attention due to their potential applications in photoelectrochemical conversion,[9,10] photovoltaic devices,[11–14] lithium-ion batteries,[4,7,8,15–17] gas sensors,[6,18,19] and high-density nanoelectronic technologies.[20,21] Here the morphology is of particular relevance. For example, when used as the electron transport layer for photovoltaic devices, the nanoscale morphology will affect the charge carrier transport and thereby the device efficiency.[22] Current lithographic techniques employed in the microelectronic industry face the escalating production cost by further decreasing the feature size.[23–25] As an inexpensive alternative, the block copolymer templated sol-gel method can achieve various nanoscale structures with the assistance of self-assembly of block copolymers.[2,20,26–30] Typically, nanopatterning of the Fe_2O_3 NPs through block copolymer templates can be categorized into two types: directly accommodating the NPs inside the block copolymer matrix or in situ reducing block copolymer coordinated metal precursors into NPs. To accommodate the NPs, a special surface treatment of the NPs

S. Yin, W. Cao, N. Li, C. L. Weindl, Prof. P. Müller-Buschbaum
Lehrstuhl für Funktionelle Materialien
Physik-Department
Technische Universität München
James-Franck-Str. 1, 85748 Garching, Germany
E-mail: muellerb@ph.tum.de

Dr. Q. Ji, Prof. Y. Cheng
Ningbo Institute of Materials Technology and Engineering
Chinese Academy of Sciences
1219 Zhongguan West Rd, Ningbo 315201, P. R. China

The ORCID identification number(s) for the author(s) of this article can be found under https://doi.org/10.1002/admi.202100141.

DOI: 10.1002/admi.202100141

Prof. L. Song
Frontiers Science Center for Flexible Electronics
Xi'an Institute of Flexible Electronics (IFE) and
Xi'an Institute of Biomedical Materials & Engineering
Northwestern Polytechnical University
127 West Youyi Road, Xi'an 710072, China

Dr. M. Schwartzkopf, Prof. S. V. Roth
Deutsches Elektronen-Synchrotron DESY
Notkestr. 85, 22603 Hamburg, Germany

Prof. S. V. Roth
Department of Fibre and Polymer Technology
KTH Royal Institute of Technology
Teknikringen 56-58, SE-100 44 Stockholm, Sweden

Prof. P. Müller-Buschbaum
Heinz Maier-Leibnitz Zentrum (MLZ)
Technische Universität München
Lichtenbergstr. 1, 85748 Garching, Germany

for a proper dispersion in the block copolymer is required. For example, Barandiaran and Kortaberria[1] modified Fe_2O_3 maghemite NPs with polystyrene (PS) brushes and prepared hybrid polystyrene-block-poly(4-vinyl pyridine) (PS-b-P_4VP)/Fe_2O_3 nanocomposites with tailored magnetic properties. The morphology change of the neat and composite thin films was systematically investigated with respect to a dioxane vapor annealing time. Abul Kashem et al.[31] prepared a series of polystyrene-block-polyisoprene/maghemite NPs (PS-b-PI/Fe_2O_3) composite thin films by grafting PS chains on to maghemite NP surface and studied the structural evolution of the thin film structures with respect to the NP concentration. Yao et al.[32] controlled the alignment of polystyrene coated maghemite NPs within a block copolymer matrix by employing different external magnetic fields. The nano- and microstructure and the magnetic behavior of the hybrid films were investigated as a function of the NP concentration. Emrick et al.[33] modified CdSe NPs with trioctylphosphine oxide (TOPO) and polyethylene glycol polymer, which allowed for the specific location of the NPs in the PS and P_2VP domains of the block polymer PS-b-P_2VP. However, this method involves sophisticated NP preparation and modification processes and serious NP agglomeration can be provoked through a high loading of the polymer matrix with NPs. In the case of the in situ reduction approach, the metal precursors are specifically cooperated in one domain of the block copolymer and the metal oxide NPs can be obtained by removing the organic species with pyrolysis or oxygen plasma treatment. Accordingly, the complex surface modification of the NPs is circumvented. For example, Hardy et al.[5] synthesized highly ordered iron oxide NPs (α-Fe_2O_3) through well-defined ferrocene-containing triblock copolymers by UV/ozonolysis and thermal pyrolysis. Sohn et al.[2] realized the concurrent self-assembly of gold and iron oxide NPs by adding dodecanethiol-protected gold NPs and $FeCl_3$ to the toluene solution of PS-b-P_4VP micelles. To the best of our knowledge, the polymer concentration and the solvent effect for block copolymer templated α-Fe_2O_3 thin film synthesis has been rarely investigated. Related research in our group demonstrated the prominent influence of the PS-b-P_4VP concentration on the ZnO morphology and the solvent effect during the polystyrene-block-polyethylene oxide (PS-b-PEO) templated TiO_2 and SnO_2 synthesis.[26,34,35]

The formation of thermodynamically stable block polymer micelles is mainly governed by the following three contributions: The stretching degree of the core-forming polymer chains, the interfacial tension between the micelle core and the surrounding solvent, and the repulsive interactions among corona-forming chains.[25] The first two contributions can be affected by factors including copolymer composition and concentration, poor solvent content in the solution, and the preferential affinity of the common solvent.[36] The third contribution mainly refers to block polymers, which contain easily ionized chains during micellization. In this situation, the electrostatic repulsions among the polymer chains turn out to be the major component affecting the micellar structures. Accordingly, the morphology control for this kind of block polymer can be realized via the addition of acids, bases, or salts, such as HCl, NaOH, or NaCl, etc.[37]

In the present work, the PS-b-P_4VP diblock copolymer templated α-Fe_2O_3 thin film synthesis is systematically investigated in terms of the solvent category and PS-b-P_4VP concentration. Two kinds of solvents with different preferential affinities to the polymer blocks (DMF and 1,4-dioxane) and three diblock copolymer (PS-b-P_4VP) to precursor ($FeCl_3$) weight ratios ($\omega_{PS\text{-}b\text{-}P4VP}$:$\omega_{FeCl3}$) are used for the solution preparation. Moreover, a series of DMF/1,4-dioxane mixtures with different compositions are confected for tuning the preferential affinity of the solvent for tracking the continuous evolution of the nanostructures. Due to keeping the $FeCl_3$ concentration in each sol-gel stock solution identical, the influence of the ionization of the P_4VP chains on the thin film morphology is ignored in the following analysis. The phase composition of the thin films is determined by X-ray diffraction (XRD), Raman spectroscopy, and X-ray photoelectron spectroscopy (XPS). The surface and inner film morphologies are probed with scanning electron microscopy (SEM) and grazing-incidence small-angle X-ray scattering (GISAXS), respectively. Based on the multidimensional characterization results, the underlying mechanism for governing the structural evolution of the thin films is revealed.

2. Experimental Section

2.1. Materials

Poly(styrene-b-4-vinyl pyridine) (PS-b-P_4VP) was obtained from Polymer Source Inc. with a molecular weight of 11.8 kDa for the PS block and 10.8 kDa for the P_4VP block. The polydispersity index (PDI) of the PS-b-P_4VP polymer was 1.12. Iron (III) chloride 97%, N, N-dimethylformamide (DMF, anhydrous, 99.8%), 1,4-dioxane (99.8%), were purchased from Sigma-Aldrich and used directly without further treatment.

2.2. Sample Preparation

The preparation routine of PS-b-P_4VP templated α-Fe_2O_3 thin films is schematically shown in **Figure 1**a. For the sol-gel stock solution preparation, 2 mL solvent (DMF or 1,4-dioxane) was equally divided into two portions for dissolving $FeCl_3$ powder and PS-b-P_4VP polymer, respectively. 20 mg $FeCl_3$ powder was weighed in a N_2 glove box to get rid of the effect of moisture in the air. After being taken out from the glove box, the $FeCl_3$ powder was dissolved with 1 mL solvent (DMF or 1,4-dioxane). Meanwhile, PS-b-P_4VP polymer solutions with different concentrations were prepared by dissolving 10 mg, 20 mg, or 40 mg PS-b-P_4VP into 1 mL of the same solvent. The prepared $FeCl_3$ and PS-b-P_4VP solutions were stirred for 1 h for complete dissolution. Afterwards, the $FeCl_3$ and polymer solutions were mixed and followed by further stirring for one hour to incorporate the inorganic $FeCl_3$ part into the micellar structures of the PS-b-P_4VP. Three $\omega_{PS\text{-}b\text{-}P4VP}$:$\omega_{FeCl3}$ ratios with fixed $FeCl_3$ concentrations, 1:2, 1:1, and 2:1, were used for investigating the polymer concentration effect in each solvent system. The component phase diagram of the different sol-gel solutions is shown in Figure S1 (Supporting Information). Figure S2 (Supporting Information) refers to the photograph of the prepared $FeCl_3$ and PS-b-P_4VP/$FeCl_3$ sol-gel solutions. Via complexation between iron ions and the applied organic solvents (as sketched

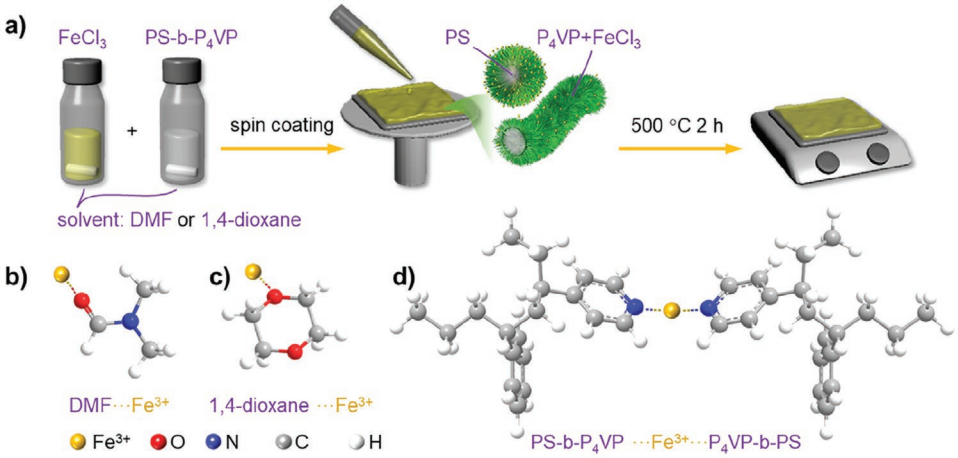

Figure 1. a) Preparation routine of PS-b-P_4VP templated α-Fe_2O_3 thin films. Sketches of the complexation between $FeCl_3$ and solvent molecules: b) DMF···Fe^{3+} complex and c) 1,4-dioxane···Fe^{3+} complex. Complexation between d) $FeCl_3$ and PS-b-P_4VP polymer template. Chlorine atoms are omitted for clarity of the presentation.

in Figure 1b,c), the black-brown $FeCl_3$ powders were completely dissolved and clear solutions were obtained. In addition, no precipitates were observed after mixing the $FeCl_3$ and PS-b-P_4VP solutions. For the sol-gel solutions prepared with DMF/1,4-dioxane solvent mixture, 40 mg PS-b-P_4VP and 20 mg $FeCl_3$ ($\omega_{PS\text{-}b\text{-}P4VP}$:$\omega_{FeCl3}$ = 2:1) were first dissolved with 1 mL DMF/1,4-dioxane solvent mixture, respectively. Then, the sol-gel solution was prepared with the same routine as the pure solvent counterpart. For the thin film deposition, the prepared sol-gel solutions were spin-coated on pre-cleaned silicon substrates with a Delta 6 RC TT spin coater (SÜSS Micro-Tec Lithography GmbH) at 2000 rpm for 60 s. To remove the polymer template, the spin-coated thin films were calcined at 500 °C for 2 h with a heating rate of 1 °C min^{-1} under ambient atmosphere. Due to the preferential affinity of the solvent to the polymer blocks, various micellar structures formed in the sol-gel stock solution. Moreover, the vinyl pyridine side group on the P_4VP chain has one free electron pair that is not involved in bonding and therefore can bind or react with Fe^{3+} ion as a good ligand.[38] Accordingly, the Fe^{3+} species can be confined in the P_4VP domains through complexation (Figure 1d). By calcining the spin-coated thin films in air, the polymer template PS-b-P_4VP is removed and mesoporous α-Fe_2O_3 films formed simultaneously.

2.3. Thin Film Characterization

The crystallinity of the α-Fe_2O_3 thin films was studied with a D8 ADVANCE X-ray diffractometer using an X-ray wavelength of 1.54 Å. Raman spectra were acquired with an "inVia Reflex Raman System," which consisted of a research-grade optical microscope (Leica DM2700M, Magnification 5×, 20×, 50×) and a high-performance Raman spectrometer (Renishaw). For both, the XRD and Raman characterization, drop-casting was used for the film preparation to increase the measurement signal. X-ray photoelectron spectroscopy (XPS) measurements were performed with an ESCALAB 250Xi spectrometer (monochromatized Al Kα radiation, h_v = 1486.6 eV) at ambient conditions. The surface morphology of the α-Fe_2O_3 thin films was probed with a high-resolution field emission scanning electron microscope (SEM, Zeiss Gemini NVision 40) at a working distance of 3.5 mm and an acceleration voltage of 5 kV. Grazing-incidence small-angle X-ray scattering (GISAXS) measurements for all samples were performed at the P03 beamline of PETRA III storage ring.[39] The wavelength and incidence angle used for the measurement was 0.96 Å and 0.35°, respectively. The sample to detector distance was 4340 mm and a Pilatus 300K (Dectris Ltd.) detector with a pixel size of 172 µm was used for recording the scattering signal. A python program called Directly Programmable Data Analysis Kit (DPDAK) was used for calibration and data analysis.[40]

3. Result and Discussion

3.1. Phase Composition

Figure 2a shows the XRD patterns of the thin films with diffraction peaks at 24.2°, 33.3°, 41.0°, 49.5°, 54.2°, and 57.6° corresponding to the (012), (104), (110), (113), (124), (116) and (122) lattice planes of the rhombohedral hematite (α-Fe_2O_3, JCPDS NO. of 01-1053).[41] The XRD characterization indicates that the crystallinity of the thin films is almost unaffected by the utilized solvent or $\omega_{PS\text{-}b\text{-}P4VP}$:$\omega_{FeCl3}$ ratios. Besides the XRD characterization, the phase composition of the calcined thin films is further confirmed by the Raman spectra. The vibrational modes of hematite at the first Brillouin zone center can be represented by

$$\Gamma_{vib} = 2A_{1g} + 2A_{1u} + 3A_{2g} + 2A_{2u} + 5E_g + 4E_u \quad (1)$$

The A_{1u} and A_{2g} modes in the equation are acoustic and optically silent. The remaining symmetrical (g) modes are active in Raman, and the asymmetrical (u) ones are active in infrared (IR) spectra. Figure 2b shows the Raman spectra of the calcined thin films prepared with different solvents and $\omega_{PS\text{-}b\text{-}P4VP}$:$\omega_{FeCl3}$ ratios. The peak located at 221 cm^{-1} corresponds to A_{1g} mode and the remaining two peaks at 288 and 405 cm^{-1} are attributed to the E_g modes.[10,42] The appearance of these three

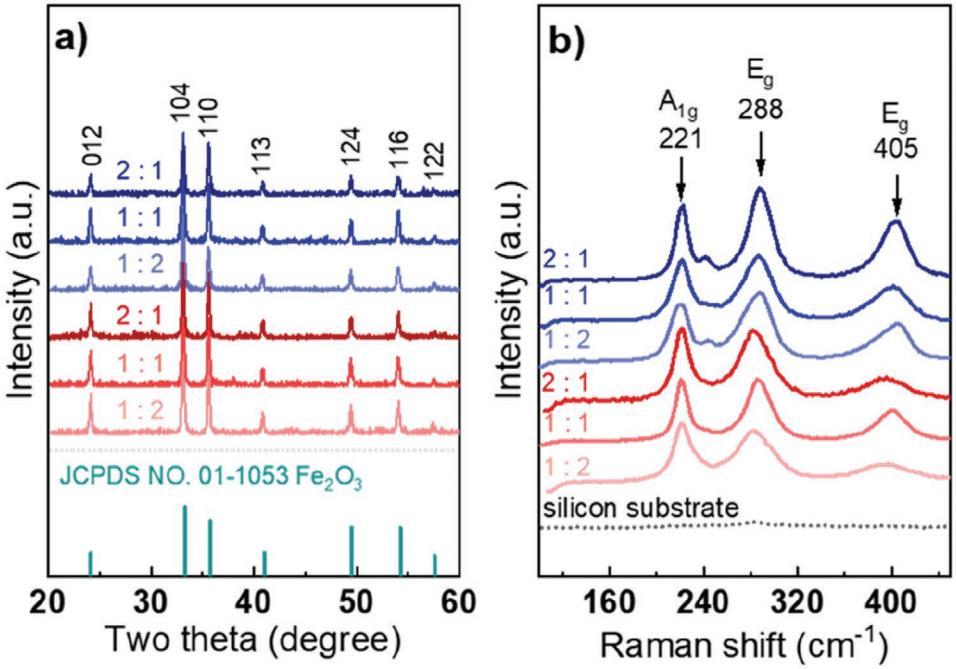

Figure 2. a) Powder XRD data and b) Raman spectra of the α-Fe_2O_3 thin films prepared with DMF (red lines) and 1,4-dioxane solvent (blue lines). The indexed Bragg peaks of rhombohedral α-Fe_2O_3 (JCPDS No. of 01-1053) are indicated with the vertical dark cyan lines at the bottom of Figure 2a. The black dash line at the bottom of Figure 2b refers to the Raman spectra of the bare silicon substrate. The $\omega_{PS\text{-}b\text{-}P4VP}$:$\omega_{FeCl3}$ ratio used for the thin film preparation is labeled above the respective XRD or Raman data.

characteristic peaks indicates that the PS-b-$P_4VP\cdots FeCl_3$ complexes in all thin films are completely converted into α-Fe_2O_3 after the calcination process.

Additionally, **Figure 3**a,b shows the core-level Fe 2p XPS spectra for the calcined thin films prepared with $\omega_{PS\text{-}b\text{-}P4VP}$:$\omega_{FeCl3}$ of 2:1 in DMF and 1,4-dioxane solvent. The major $Fe2p_{1/2}$ and $Fe2p_{3/2}$ peaks of the two samples are observed centered at 710.8 eV and 724.4 eV with a spin energy separation of 13.6 eV. The two weak peaks that appear at 718.9 and 732.4 eV correspond to the shakeup satellites of $Fe2p_{3/2}$ and $Fe2p_{1/2}$. All peaks are typical characteristics of α-Fe_2O_3.[3,43,44] Apart from the Fe 2p peaks, prominent O 1s and C 1s peaks are also clearly visible in the full-range XPS survey spectra of both thin films, which can be ascribed to the organic functional group residues of the polymeric template after calcination (Figure 3c).

3.2. Thin-Film Morphology

Figure 4a–c and Figure S4a–c (Supporting Information) show the SEM images and corresponding zoom-in view of the α-Fe_2O_3 thin films prepared with DMF solvent. The

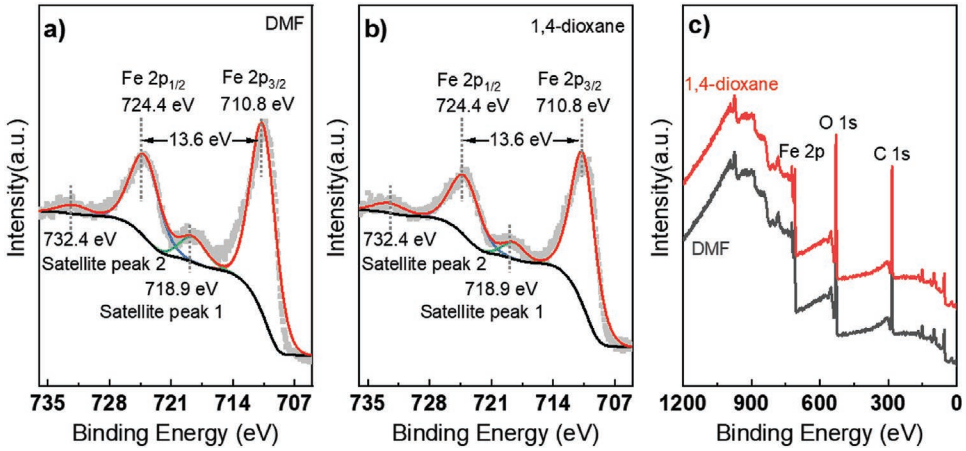

Figure 3. a,b) Core-level Fe 2p XPS spectra and c) full-range XPS survey spectra for the α-Fe_2O_3 films prepared with $\omega_{PS\text{-}b\text{-}P4VP}$:$\omega_{FeCl3}$ = 2:1 in DMF and 1,4-dioxane solvent.

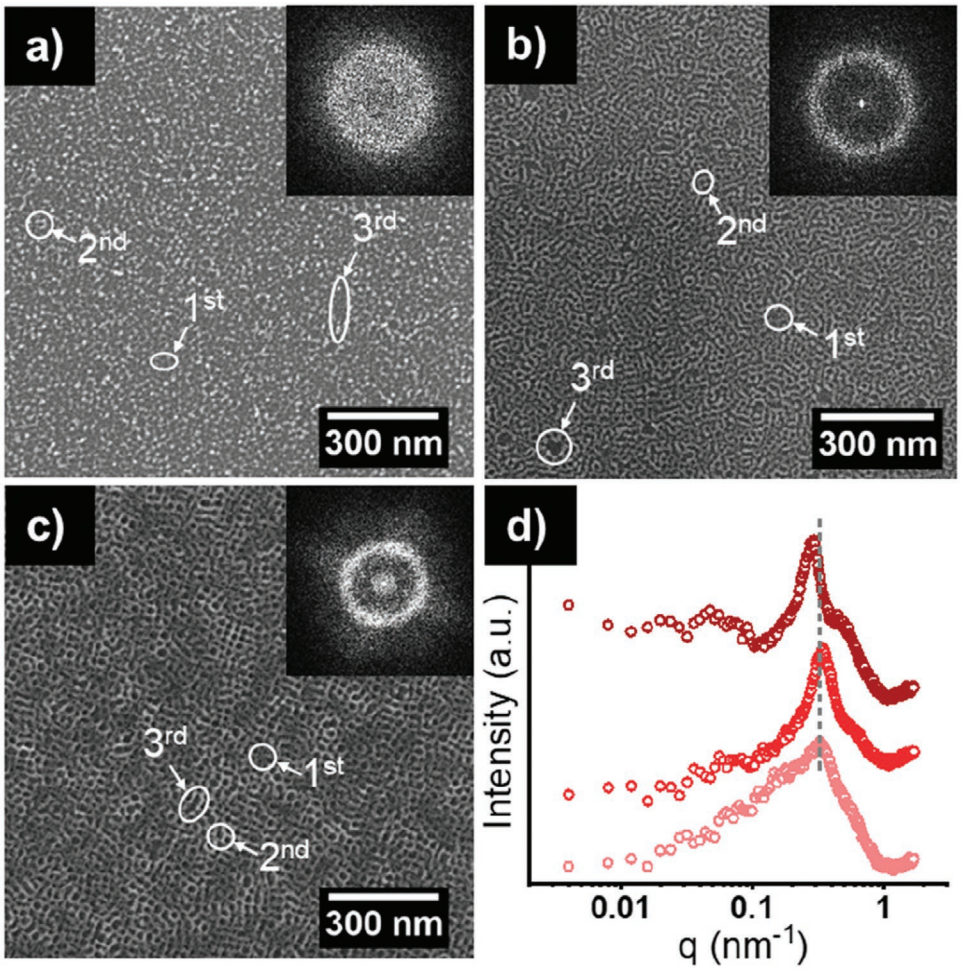

Figure 4. SEM images and corresponding fast Fourier transform (FFT) patterns of a–c) the α-Fe_2O_3 thin films prepared by DMF solvent. The $\omega_{PS\text{-}b\text{-}P4VP}$:$\omega_{FeCl3}$ ratios are a) 1:2, b) 1:1, and c) 2:1, respectively. d) In the PSD functions calculated from the SEM images, gradually darkening colors are utilized to represent the increase of the $\omega_{PS\text{-}b\text{-}P4VP}$:$\omega_{FeCl3}$ ratio from 1:2 to 2:1. The gray dashed line in (d) is as a guide to the eye and the first, second, and third nanostructures used for the GISAXS data modeling are marked with white circles in a–c. For clarity, the zoom-in view of the nanostructures is presented in Figure S4 (Supporting Information).

corresponding $\omega_{PS\text{-}b\text{-}P4VP}$:$\omega_{FeCl3}$ values used for the thin film preparation are 1:2, 1:1, and 2:1 for Figure 4a–c, respectively. The thin film prepared with $\omega_{PS\text{-}b\text{-}P4VP}$:$\omega_{FeCl3}$ of 1:2 is mainly composed of small nanoclusters (Figure 4a). When increasing the $\omega_{PS\text{-}b\text{-}P4VP}$:$\omega_{FeCl3}$ ratio to 1:1, a nanopattern consisting of spherical pore structures is formed. The porous structure of the thin film is directly associated with the template effect of the micelles in the solution. Due to the preferential affinity of the DMF solvent to the P_4VP chains, spherical micelles consisting of PS cores and P_4VP/Fe^{3+} coronas are prone to be formed, no matter in the DMF solution or the final dry film. The structural transition from nanoclusters to the patterned nanostructures can be related to the micellization of the PS-b-P_4VP template at the critical concentration, which is proportional to the concentration of the block copolymer. However, the formed micellar structures are labile at the early stage of the micellization due to the highly swollen condition of the core-forming chains by the solvent, which provides a strong probability for micelle fusion. This fusion might account for the existence of the secondary large pore structures seen in Figure 4b.[45] By further increasing the $\omega_{PS\text{-}b\text{-}P4VP}$:$\omega_{FeCl3}$ ratio to 2:1, a more uniform distribution of the pore structures and a slight increase of the pore size are observed within the thin film (Figure 4c). The influence of copolymer concentration on the micellar morphology can be tentatively explained by the equation from a theory for small-molecule surfactant micelles.[25]

$$N_{agg} = 2(C/\mathrm{CMC})^{1/2} \quad (2)$$

N_{agg} is the average number of polymer chains in an aggregate, C represents the copolymer concentration and CMC is the copolymer concentration at the critical water content. As seen in Equation (2), N_{agg} is proportional to the copolymer concentration C. For spherical micelles, the increase of the N_{agg} value yields larger core dimensions and an increase in the stretching degree of the core-forming blocks. This process is energetically favorable because the formation of a larger core size decreases the aggregate number and the total interfacial area within the system. Cross-section images of the α-Fe_2O_3 thin films are

shown in Figure S3 (Supporting Information). It is observed that all the thin films are composed of a mesoporous α-Fe_2O_3 monolayer. Figure 4d shows the corresponding power spectral density (PSD) functions extracted from the SEM images. The enhanced ordering of the nanostructures can be manifested in the FFT patterns by the appearance of a sharp peak in the PSD functions. The sharp peaks of the PSD functions show the q values of the most dominant lateral feature sizes in the SEM images.[46] Specifically, the peak values of the thin films prepared with $\omega_{PS\text{-}b\text{-}P4VP}$:$\omega_{FeCl3}$ ratios of 1:2, 1:1, and 2:1 are determined to be 0.31, 0.34, and 0.28 nm^{-1}, which correspond to feature sizes of 20.3, 18.5, and 22.4 nm, respectively. The system correlation length is a measure for the lateral ordering of structures within the thin film, which is inversely proportional to the full width at half maximum (FWHM) of the first-order peak of the PSD functions.[47] The calculated correlation lengths for the nanostructures shown from Figure 4a–c are 4.8, 10.4, and 14.3 nm, which demonstrate the enhanced ordering with the increase of the $\omega_{PS\text{-}b\text{-}P4VP}$:$\omega_{FeCl3}$ ratio.

With the SEM measurements, the local structure on the film surface is probed. However, in practical applications, the large area homogeneity and the inner structure of the thin film are also of great importance. Grazing-incidence small-angle X-ray scattering (GISAXS) ideally complements microscopic imaging techniques as it readily provides statistical structure information at both, the surface and the bulk of the thin film.[48] **Figure 5**a–c shows the 2D GISAXS data of the α-Fe_2O_3 thin films prepared with DMF solvent. The shape of the Bragg peaks indicates the presence of well-ordered nanostructures in the horizontal direction of the thin films.[49] To extract the lateral structure information within the thin films, horizontal line cuts are performed at the material characteristic Yoneda peak as indicated by the white arrow in Figure 5a. Figure 5d shows the horizontal line cuts of the 2D GISAXS data. The additional broad peak in the low q_y region for the thin film prepared with $\omega_{PS\text{-}b\text{-}P4VP}$:$\omega_{FeCl3}$ of 1:1 can be assigned to the existence of the fused large pore structures within the film. Moreover, the shift of the most pronounced scattering peaks in Figure 5d is in good accordance with the behavior of the PSD functions, which qualitatively reflects that the prepared thin films possess the same structural evolution trend within the local and large probed area. For quantitatively extracting the in-plane structure information of the α-Fe_2O_3 thin films, the horizontal line cuts in Figure 5d are fitted within the framework of the distorted-wave Born approximation (DWBA) using a local monodisperse approximation (LMA).[50] In the modeling, Gaussian distributed form factors and structure factors are assumed.[51] The form factors denote the shape and size of the scattering objects, which is assumed to be standing cylinders, and the structure factors refer to the center-to-center distances between the scattering objects in a 1D paracrystal arrangement, respectively. For more details, see Supporting Information. Error bars indicate the scope of the goodness of fit. The fitted radii and distances are shown in Figure 5e,f. The most conspicuous scattering peak in the high q region is fitted to extract the second structure information. When the $\omega_{PS\text{-}b\text{-}P4VP}$:$\omega_{FeCl3}$ ratio increase from 1:2 to 2:1, the center-to-center distances of the second structure are determined to be (20.0 ± 1.4), (17 ± 3), and (22 ± 2) nm. The fitted center-to-center distances are in good agreement with the feature sizes calculated from the main peak of the PSD functions, which reflects a good consistency of the main feature sizes in the local and large probed areas of the thin film. In addition, the corresponding radii of the second structure are fitted to be (5.6 ± 0.3), (4.5 ± 0.4), and (5.0 ± 0.4) nm. Based on the fitted center-to-center distances and radii, the pore sizes formed by the nanostructures can be calculated with the approach[34,52]

$$\text{Pore size} = \text{center}-\text{to}-\text{center distance} - (2 \times \text{structure radius}) \quad (3)$$

Considering that the thin film prepared with a $\omega_{PS\text{-}b\text{-}P4VP}$:$\omega_{FeCl3}$ ratio of 1:2 is mainly composed of discrete nanoclusters and no distinct pore structures can be observed, the pore size calculation is only performed for the other two samples. Accordingly, the pore sizes calculated from the second center-to-center distances and radii are (8 ± 4) and (12 ± 3) nm for the thin films prepared with $\omega_{PS\text{-}b\text{-}P4VP}$:$\omega_{FeCl3}$ of 1:1 and 2:1. In addition, the weak scattering intensity in the higher q_y region for all line cuts is fitted with a smaller first center-to-center distance and radius. The first center-to-center distances for the thin films prepared with $\omega_{PS\text{-}b\text{-}P4VP}$:$\omega_{FeCl3}$ ratios of 1:2, 1:1, and 2:1 are determined to be (10.0 ± 1.5), (8.6 ± 0.9), and (11.0 ± 1.2) nm, and the corresponding radii are fitted to be (2.6 ± 0.5), (2.3 ± 0.4), and (2.6 ± 0.5) nm. According to Equation 3, the first pore sizes are calculated to be (4.0 ± 1.7) and (6 ± 2) nm for the thin films prepared with $\omega_{PS\text{-}b\text{-}P4VP}$:$\omega_{FeCl3}$ of 1:1 and 2:1. Moreover, the additional broad peak in the low q_y region for all thin films is fitted with a third distance and radius. Specifically, the center-to-center distance of the thin films prepared with $\omega_{PS\text{-}b\text{-}P4VP}$:$\omega_{FeCl3}$ ratios of 1:2, 1:1, and 2:1 is determined to be (210 ± 25), (90 ± 19), and (120 ± 18) nm, and the corresponding radius is determined to be (6.5 ± 0.5), (5.0 ± 0.5), and (5.5 ± 0.5) nm, respectively. The pore sizes generated by the third structure are calculated to be (80 ± 20) and (109 ± 19) nm for the thin films prepared with $\omega_{PS\text{-}b\text{-}P4VP}$:$\omega_{FeCl3}$ of 1:1 and 2:1. The small and large pore sizes calculated from the first and third structure factors can be ascribed to the locally collapsed or fused large pore structures within the thin film. Notably, all the modeled feature sizes in the GISAXS data analysis can be identified with surface features in the SEM images (Figure 4). The good consistency between the GISAXS fit results and the SEM topography demonstrates that the nanostructures observed within the micron size range extend over a larger area on the thin film.

Figure 6a–c and Figure S5a–c (Supporting Information) show the SEM images and corresponding zoom-in view of the α-Fe_2O_3 thin films prepared with 1,4-dioxane. Compared with the DMF counterpart samples, completely different morphologies are observed in the 1,4-dioxane system. When the $\omega_{PS\text{-}b\text{-}P4VP}$:$\omega_{FeCl3}$ ratio is 1:2, discrete nanoclusters accompanied with large aggregates are observed. By increasing the $\omega_{PS\text{-}b\text{-}P4VP}$:$\omega_{FeCl3}$ ratio to 1:1 and 2:1, uniformly distributed worm-like structures with enhanced order, as verified by the FFT patterns, are formed. Figure 6d shows the corresponding PSD functions calculated from the SEM images. Due to the polydispersity of the nanostructures, no distinct peak is observed in the PSD function of the thin film prepared with a $\omega_{PS\text{-}b\text{-}P4VP}$:$\omega_{FeCl3}$ ratio of 1:2. The sharp peaks shown in the other

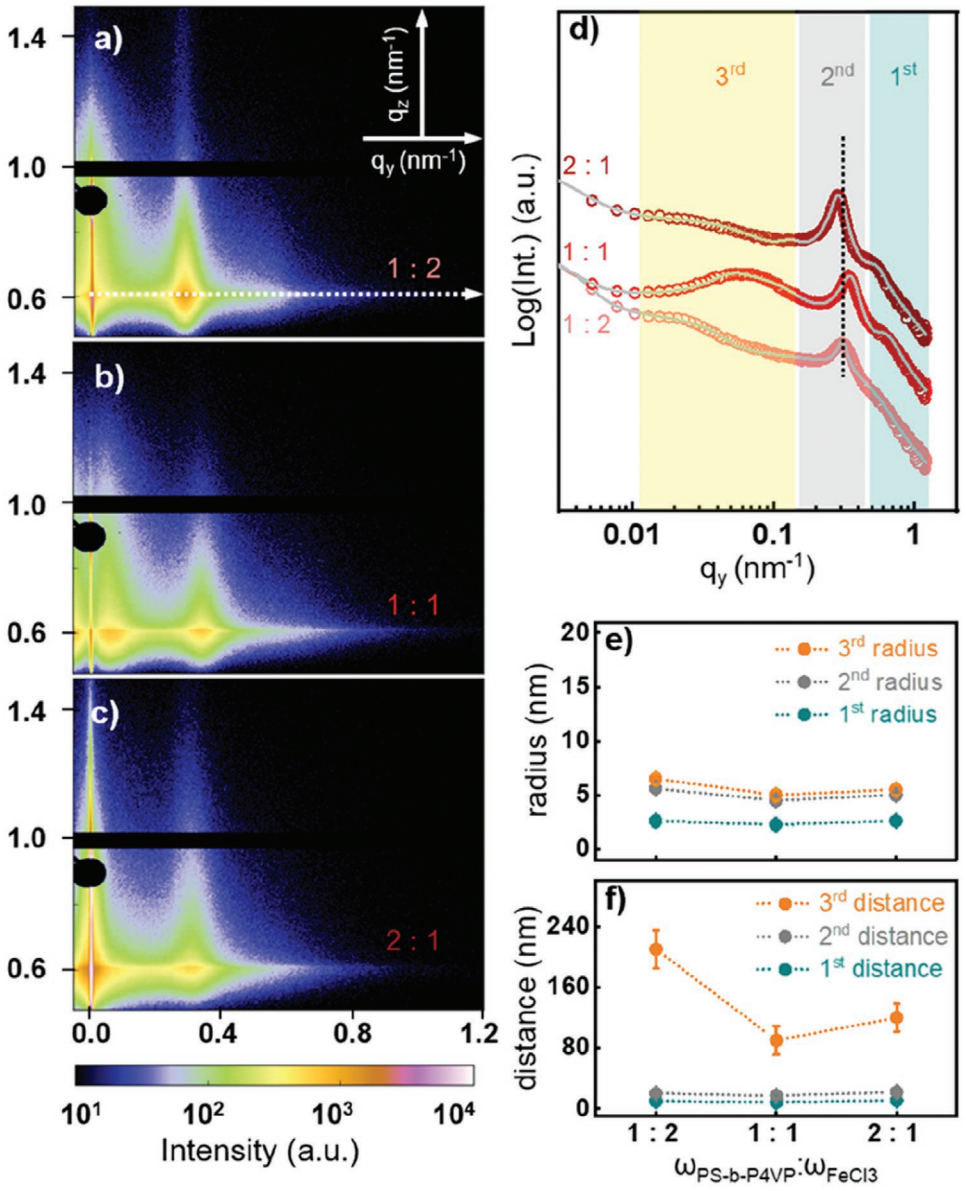

Figure 5. a–c) 2D GISAXS data and d) corresponding horizontal line cuts of the thin films prepared with DMF solvent. The $\omega_{PS\text{-}b\text{-}P4VP}$:$\omega_{FeCl3}$ ratios used for sample preparation are noted in the lower right corner of the 2D GISAXS data and the left side of the horizontal line cuts. The position for performing horizontal cuts is denoted as a white arrow in (a). The black dashed line in (d) is plotted as a guide to the eye. The scattering peaks appearing in the high, medium, and low q_y regions are marked with cyan, grey and yellow rectangles, respectively. e) The radii and f) center-to-center distances for the different thin films are determined from the fits.

two PSD functions can be used for determining the feature sizes and order. The peak centers of the thin films prepared with $\omega_{PS\text{-}b\text{-}P4VP}$:$\omega_{FeCl3}$ ratios of 1:1 and 2:1 are determined to be 0.23 and 0.24 nm^{-1}, which corresponds to feature sizes of 27.3 and 26.2 nm, respectively. The FWHM of the thin films prepared with $\omega_{PS\text{-}b\text{-}P4VP}$:$\omega_{FeCl3}$ ratios of 1:1 and 2:1 are determined to be 0.11 and 0.13 nm^{-1}, which corresponds to correlation lengths of 9.1 and 7.7 nm, respectively. The fitted peak position and calculated correlation lengths indicate that both, the feature sizes and order of the thin films are decreased by increasing the $\omega_{PS\text{-}b\text{-}P4VP}$:$\omega_{FeCl3}$ ratios from 1:1 to 2:1. The drastic morphology variation of the thin films with respect to the solvent category can be tentatively explained by a preferential affinity of the solvent to the polymer blocks. Based on the characteristic parameters of the different polymers and solvents, the polymer–solvent interaction parameters (χ_{P-S}) is calculated via

$$\chi_{P-S} = \frac{V_s(\delta_S - \delta_P)^2}{RT} + 0.34 \quad (4)$$

V_S refers to the molar volume of the solvent, δ_S, and δ_P are the solubility parameter of the solvent and the polymer, respectively. R and T are the gas constant and temperature, respectively. According to the literature, the δ_H of PS and P_4VP blocks are 18.6

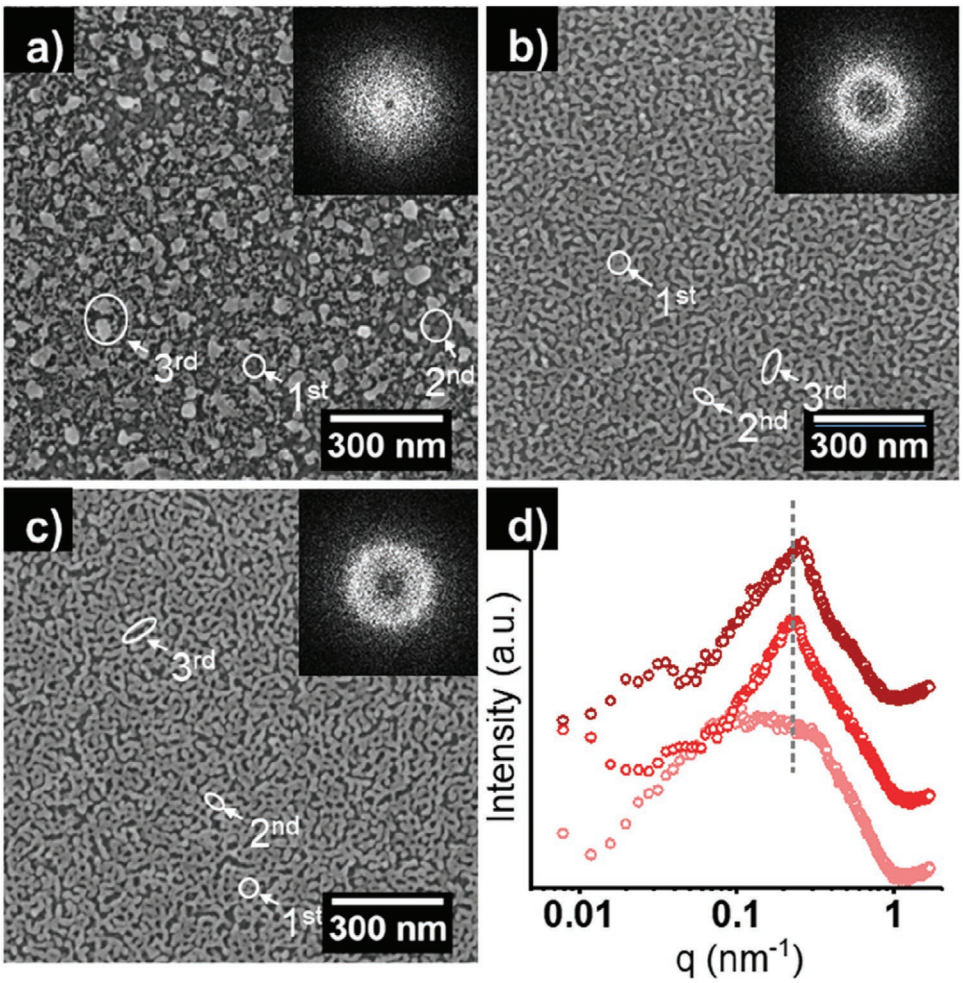

Figure 6. SEM images and corresponding fast Fourier transform (FFT) patterns of the α-Fe_2O_3 thin films prepared with a–c) 1,4-dioxane solvent. The corresponding $\omega_{PS\text{-}b\text{-}P4VP}$:$\omega_{FeCl3}$ ratios are a) 1:2, b) 1:1, and c) 2:1, respectively. d) In the PSD functions calculated from the SEM images, gradually darkening colors are utilized to represent the increase of $\omega_{PS\text{-}b\text{-}P4VP}$:$\omega_{FeCl3}$ ratio from 1:2 to 2:1. The first, second, and third nanostructures used for the GISAXS data modeling are marked with white circles in (a–c). For clarity, the zoom-in view of the nanostructure is presented in Figure S5 (Supporting Information).

and 23.0 $MPa^{1/2}$, respectively.[53] **Table 1** shows the Hansen solubility parameters (δ_H) of DMF and 1,4-dioxane solvents. The δ_H is calculated from a dispersive δ_d, permanent dipole–dipole interaction δ_p, and hydrogen bonding forces δ_h via

$$\delta_H^2 = \delta_d^2 + \delta_p^2 + \delta_h^2 \quad (5)$$

Table 2 are the corresponding χ_{P-S} values calculated by Equation (4). According to the Flory-Huggins theory, the polymer and solvent are completely miscible when $\chi_{P\text{-}S}$ is less than 0.5. The preferential affinity of the solvent to a certain block can be calculated by the difference between the $\chi_{PS\text{-}S}$ and $\chi_{P4VP\text{-}S}$

$$\Delta\chi = \chi_{PS-S} - \chi_{P4VP-S} \quad (6)$$

The calculated $\Delta\chi$ for the PS-b-P_4VP/DMF and PS-b-P_4VP/1,4-dioxane polymer–solvent pairs are 1.1 and –0.09. The high $\Delta\chi$ value of PS-b-P_4VP/DMF reflects the inferior solubility of the PS blocks in DMF, which leads to the significantly inhibited stretching of the PS blocks and thus promotes the formation of spherical PS micellar cores. However, the slightly negative $\Delta\chi$ value of PS-b-P_4VP/1,4-dioxane polymer-solvent pair indicates that the 1,4-dioxane has a very slight preferential affinity to the PS block. Accordingly, the appearance of the aggregates in Figure 6a and the wormlike structures in Figure 6b,c can be ascribed to the weak selectivity of 1,4-dioxane and an enhanced stretching of the PS blocks. In addition, the inter-domain distance of the wormlike

Table 1. Characteristic parameters of the DMF and 1,4-dioxane solvent.

Solvent	δ[$MPa^{1/2}$]				V_s[cm^3 mol^{-1}]
	δ_H	δ_d	δ_p	δ_h	
DMF	24.8	17.4	13.7	11.3	77.0
1,4-dioxane	20.5	19.0	1.8	7.4	85.7

Table 2. Polymer-solvent interaction parameters ($\chi_{P\text{-}S}$) of different polymer-solvent pairs.

$\chi_{P\text{-}S}$	DMF	1,4-dioxane
PS	1.54	0.47
P_4VP	0.44	0.56

structure decreases by increasing the $\omega_{PS\text{-}b\text{-}P4VP}$:$\omega_{FeCl3}$ ratio from 1:1 to 2:1, which is against the trend shown in the DMF solvent system. The decreased inter-domain distance induced by the increase of the $\omega_{PS\text{-}b\text{-}P4VP}$:$\omega_{FeCl3}$ ratio can be assigned to the unique shape of the micellar structure. It is observed that the thin films prepared with $\omega_{PS\text{-}b\text{-}P4VP}$:$\omega_{FeCl3}$ of 1:1 and 2:1 are mainly composed of interconnected wormlike structures, which is prone to deform into more elongated wormlike micelles for accommodating more polymer chains and maintaining low surface energy in the monolayer geometry.

Figure 7a–c shows the 2D GISAXS data of the α-Fe_2O_3 thin films prepared with 1,4-dioxane. Compared with the thin film prepared with a $\omega_{PS\text{-}b\text{-}P4VP}$:$\omega_{FeCl3}$ ratio of 1:2, the clearly visible Bragg rod in the lateral direction of the other two thin films can be attributed to an enhanced in-plane order of the nanostructures. Figure 6d shows the corresponding line cuts made from the 2D GISAXS data. The line cuts clearly show the sharpening of the Bragg peak by increasing $\omega_{PS\text{-}b\text{-}P4VP}$:$\omega_{FeCl3}$ ratio from 1:2 to 1:1. In addition, the Bragg peak shifts towards larger q_y values and broadens by further increasing the $\omega_{PS\text{-}b\text{-}P4VP}$:$\omega_{FeCl3}$ ratio from 1:1 to 2:1. The shift and width of the scattering peaks in

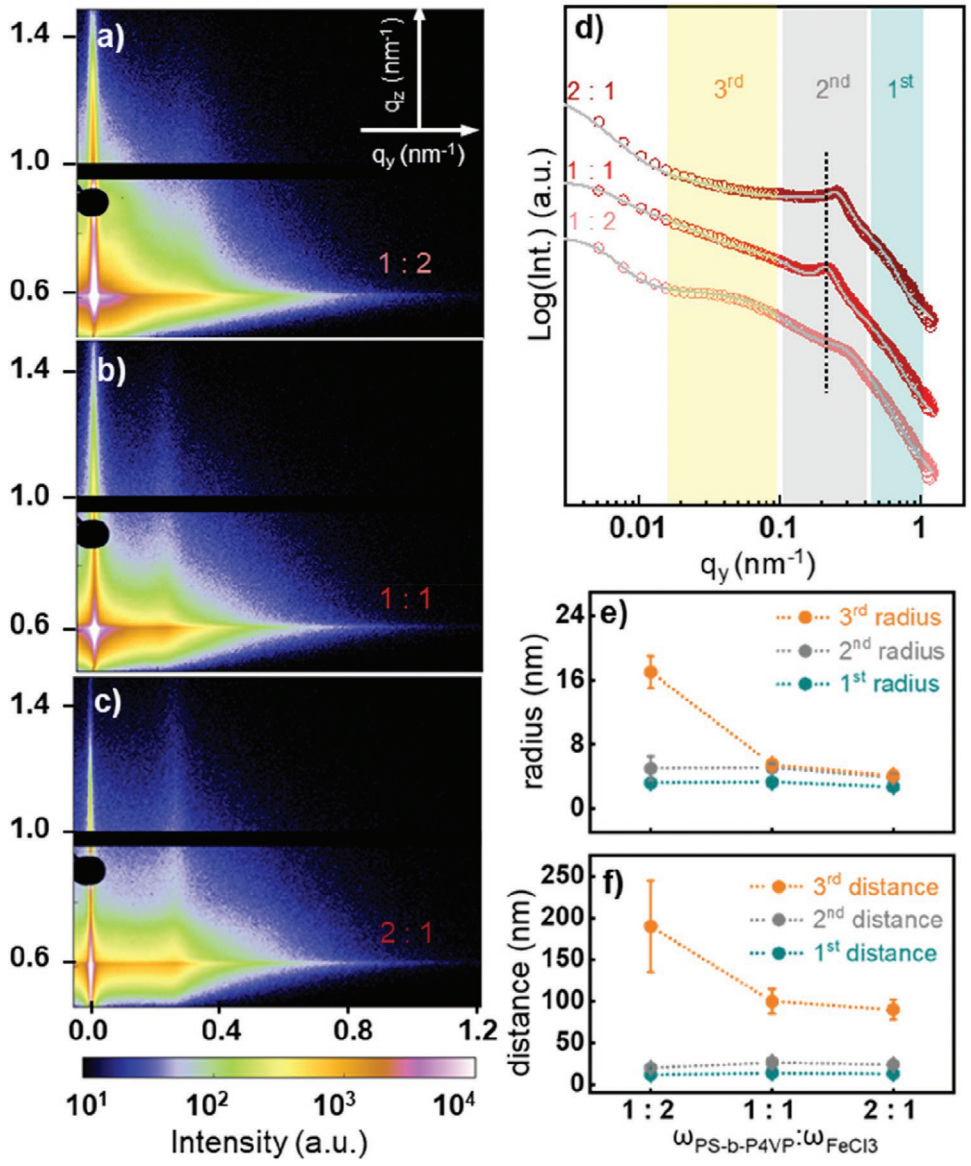

Figure 7. a–c) 2D GISAXS data and d) corresponding horizontal line cuts of the thin films prepared with 1,4-dioxane solvent, the $\omega_{PS\text{-}b\text{-}P4VP}$:$\omega_{FeCl3}$ ratios used for sample preparation are noted in the lower right corner of the 2D GISAXS data and the left side of the horizontal line cuts. The black dashed line in (d) is plotted as a guide to the eye. The scattering peaks appearing in the high, medium, and low q_y region are marked with cyan, gray, and yellow rectangles, respectively. e) The radii and f) center-to-center distances for the different thin films are determined from the fits.

Figure 7d are in good accordance with the PSD functions from Figure 6d, which demonstrates that the feature size variation trend is consistent in the local and large area of the thin film. Within the aforementioned fit model, the horizontal line cuts are fitted with three sets of nanostructures (radii and distances in Figure 7e,f). The most pronounced scattering peak in the medium q_y region is fitted with the second nanostructure. Specifically, the second distances of the thin films prepared with $\omega_{PS\text{-}b\text{-}P4VP}$:$\omega_{FeCl3}$ ratios of 1:2, 1:1, and 2:1 are determined to be (20 ± 4), (27 ± 3), and (24 ± 2) nm, which are in substantial agreement with the feature sizes calculated from the PSD functions. The corresponding radii are (5.0 ± 1.5), (5.1 ± 0.5), and (3.9 ± 0.5) nm. Based on Equation 3, the pore sizes calculated from the second distance and radii are (10 ± 7), (16 ± 4), and (16 ± 4) nm, respectively. Apart from the most conspicuous scattering signal in the medium q_y region, the weak scattering in the high and low q_y regions are fitted with the first and third nanostructures. The first center-to-center distances of the thin films prepared with $\omega_{PS\text{-}b\text{-}P4VP}$:$\omega_{FeCl3}$ ratios of 1:2, 1:1, and 2:1 are determined to be (12 ± 2), (14 ± 3), and (13 ± 2) nm and the corresponding first radius are (3.2 ± 0.2), (3.3 ± 0.3), and (2.7 ± 0.2) nm, which yields the pore sizes of (6 ± 2), (7 ± 3), and (8 ± 3) nm, respectively. Moreover, the third center-to-center distances of the thin films prepared with 1:2, 1:1, and 2:1 $\omega_{PS\text{-}b\text{-}P4VP}$:$\omega_{FeCl3}$ are determined to be (190 ± 55), (100 ± 15), and (90 ± 12) nm and the corresponding third radii are (17 ± 2), (5.5 ± 0.6), and (4.1 ± 0.6) nm, which yields the pore sizes of (156 ± 59), (89 ± 16), and (82 ± 13) nm, respectively.

3.3. Thin Film Morphology Evolution with respect to the Solvent Category and $\omega_{PS\text{-}b\text{-}P4VP}$:$\omega_{FeCl3}$ Ratios

From the discussion above, the good consistency between the SEM topography and the structures extracted in the GISAXS data analysis demonstrates that a large area homogeneity is achieved for all α-Fe_2O_3 thin films. In addition, it is clearly demonstrated that the α-Fe_2O_3 thin films prepared with a $\omega_{PS\text{-}b\text{-}P4VP}$:$\omega_{FeCl3}$ ratio of 1:2 irrespective of the solvent, in DMF and 1,4-dioxane possess similar nanocluster structures. The main structural differences caused by the solvent category consist in the distinct spherical and worm-like nanostructures formed at higher $\omega_{PS\text{-}b\text{-}P4VP}$:$\omega_{FeCl3}$ ratios. Accordingly, a schematic illustration for the micellar structure evolution, which is directly related to the α-Fe_2O_3 nanostructures, is given with respect to the different solvent category and $\omega_{PS\text{-}b\text{-}P4VP}$:$\omega_{FeCl3}$ ratios in **Figure 8**. By increasing $\omega_{PS\text{-}b\text{-}P4VP}$:$\omega_{FeCl3}$ ratio from 1:1 to 2:1, a completely different structure evolution tendency is observed for the spherical and wormlike structures. Specifically, the expansion of the spherical micelles with the increase of the $\omega_{PS\text{-}b\text{-}P4VP}$:$\omega_{FeCl3}$ ratio can be explained by the theory for small molecule surfactant micelles. The average number of polymer chains in an aggregate (N_{agg}) is proportional to copolymer concentration, and the increased N_{agg} of the spherical micelles contributes to the enhanced stretching of the core-forming blocks and therefore the expansion of the micelles. However, for the interconnected wormlike structures acquired with the 1,4-dioxane solvent, the increase of the $\omega_{PS\text{-}b\text{-}P4VP}$:$\omega_{FeCl3}$ ratio promotes the formation of more elongated wormlike micelles for accommodating more polymer chains in the monolayer geometry.

3.4. Relationship between Thin Film Morphology and $\Delta\chi$ Value of the Cosolvent

The solubility parameter of a solvent mixture can be tuned by changing its composition.[54] For tracking the successive morphology evolution with respect to the solubility parameter of a solvent, we study DMF/1,4-dioxane solvent mixtures with different compositions at a fixed $\omega_{PS\text{-}b\text{-}P4VP}$:$\omega_{FeCl3}$ ratio of 2:1 for the sol-gel solution preparation. The acquired thin film morphologies are shown in **Figure 9**. The morphology of the thin films remains almost constant when increasing the volume fraction of 1,4-dioxane from 0 to 20 vol% (Figure 9a–c). The inflection from spherical to worm-like nanostructure is triggered, when the volume fraction of 1,4-dioxane reaches 30 vol% (Figure 9d). As shown in Figure 9d, the wormlike structure appears in a form of micron-sized islands among the spherical pore structures. The formation of this unique hybrid structure is likely due to the incomplete micellar structural transformation in the sol-gel

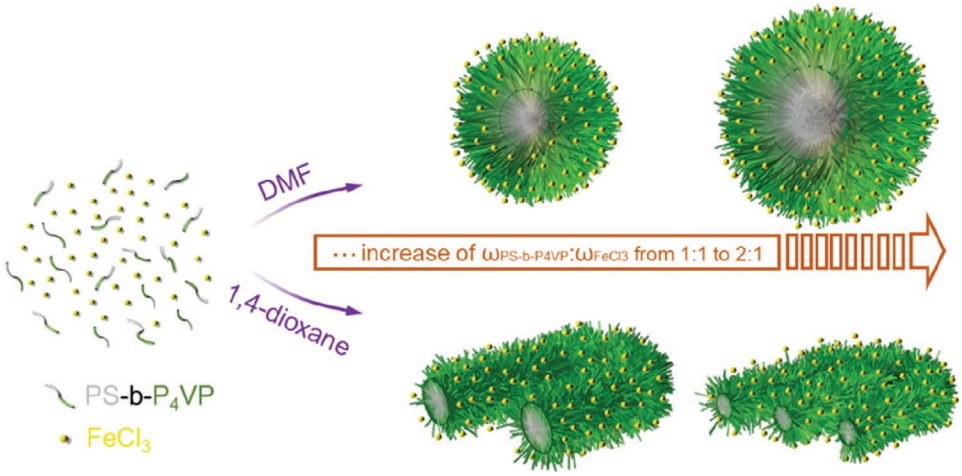

Figure 8. Schematic illustration of the micellar structures in the thin films with respect to the different solvent category and $\omega_{PS\text{-}b\text{-}P4VP}$:$\omega_{FeCl3}$ ratios.

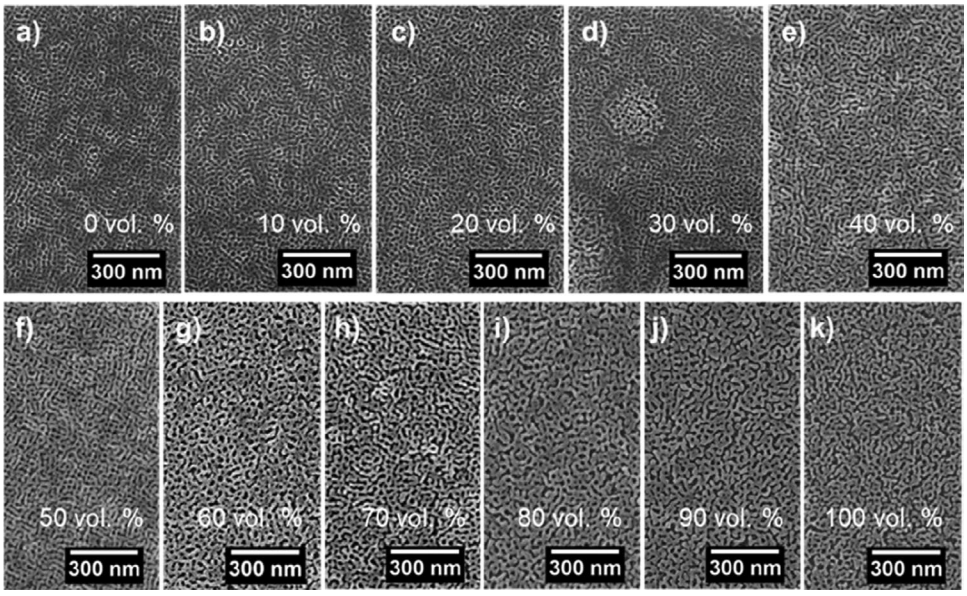

Figure 9. SEM images of the α-Fe_2O_3 thin films prepared with different DMF/1,4-dioxane ratios. The volume fraction of 1,4-dioxane in the solvent mixture are marked in the images (0 vol. % to 100 vol. % from a to k). The $\omega_{PS\text{-}b\text{-}P4VP}$:$\omega_{FeCl3}$ ratio used for solution preparation is 2:1.

solution. By further increasing the volume fraction of 1,4-dioxane from 40 to 100 vol%, the complete spherical-to-worm like micellar transformation occurs. As a result, thin films consisting of neat wormlike nanostructures are obtained (Figure 9e–k).

For unraveling the relationship between the thin film morphologies and the preferential affinity of the cosolvent, a phase diagram of the α-Fe_2O_3 thin film morphologies is plotted as a function of the volume fractions of 1,4-dioxane and the $\Delta\chi$ values of different polymer–solvent pairs (**Figure 10**). The specific polymer–solvent interaction parameters ($\chi_{P\text{-}S}$) used for the $\Delta\chi$ calculation are listed in Table S1 (Supporting Information).

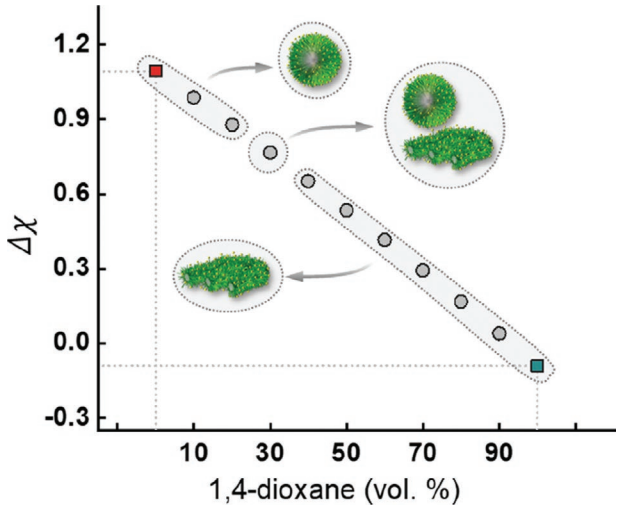

Figure 10. Phase diagram of the α-Fe_2O_3 thin film morphologies with respect to the $\Delta\chi$ values of different polymer–solvent pairs and the volume fraction of 1,4-dioxane. Pure DMF and 1,4-dioxane solvent are represented with red and dark cyan squares. DMF/1,4-dioxane solvent mixtures are denoted with gray circles. The $\omega_{PS\text{-}b\text{-}P4VP}$:$\omega_{FeCl3}$ ratio used for solution preparation is 2:1.

According to the coordinate system, the thin film morphology is primarily templated by the spherical micelle structure in the region of $0.88 \leq \Delta\chi \leq 1.09$. The spherical-to-wormlike micellar transformation occurs at the $\Delta\chi$ value of 0.77. The further decrease of the $\Delta\chi$ value from 0.65 to -0.09 yields the neat wormlike nanostructures.

In order to investigate the influence of the cosolvent compositions on the feature sizes and order of the α-Fe_2O_3 thin films, PSD functions of the SEM images from Figure 9 are calculated. As shown in **Figure 11**a, a significantly enhanced intensity in the low q region is observed for the thin film prepared with 30 vol% 1,4-dioxane. This can be ascribed to the appearance of the micron-sized islands within the thin film. Figure 11b,c refer to the corresponding peak and FWHM values extracted from the PSD functions. A progressive shift of the peak position towards smaller q values is observed by increasing the volume fraction of 1,4-dioxane from 0 to 90 vol%, which indicates the continuous expansion of the feature sizes of the pore structures. However, a slight shift of the peak position toward larger q values is observed by increasing the 1,4-dioxane volume fraction from 90 to 100 vol%. This shift is likely caused by the viscosity difference between the DMF/1,4-dioxane co-solvent and pure 1,4-dioxane.[55] In addition, the extracted FWHM values (Figure 11c) indicate that the order of the nanostructure is decreased with the increase of the volume fraction of 1,4-dioxane. The highest FWHM value of the thin film prepared with 30 vol% 1,4-dioxane can be ascribed to the mixture of the micron-sized island structures, which greatly diminishes the ordering of the thin film.

4. Conclusion

Mesoporous α-Fe_2O_3 thin films with different morphologies are synthesized by using $FeCl_3$ as precursor and the amphiphilic diblock copolymer PS-b-P_4VP as a template. The XRD, Raman,

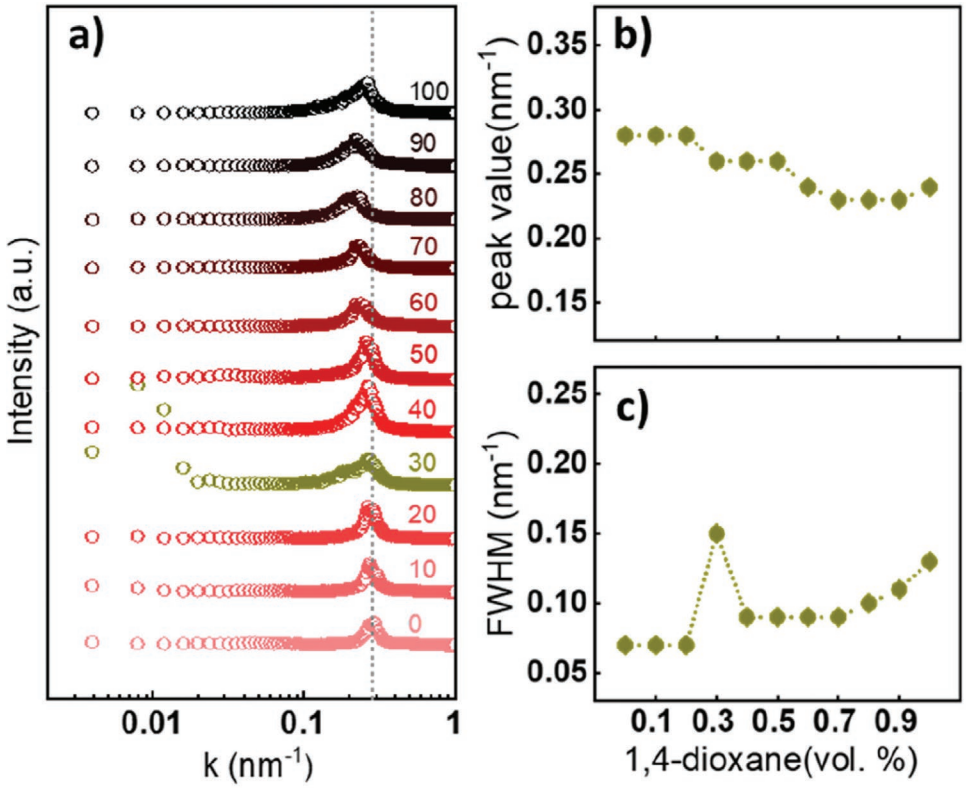

Figure 11. PSD functions of the α-Fe_2O_3 thin films prepared with a) different DMF/1,4-dioxane ratios. The volume fractions of the 1,4-dioxane are marked above each PSD function and the grey dashed line in (a) is plotted as a guide to the eye. b) The peak positions and c) FWHM for the different thin films are determined from the PSD functions.

and XPS characterization results confirm the hematite phase in all films. The morphology control at the molecular level for the thin films is realized by changing the following two factors: the solvent category and the $\omega_{PS\text{-}b\text{-}P4VP}$:$\omega_{FeCl3}$ ratio. The SEM and GISAXS characterization results demonstrate the structural consistency on the local and large areas of all thin films. When the $\omega_{PS\text{-}b\text{-}P4VP}$:$\omega_{FeCl3}$ ratio used for sol-gel solution preparation is 1:2, nanocluster structures are observed in both DMF and 1,4-dioxane solvent. This nanostructure can be assigned to the weak templating effect of the low PS-b-P_4VP concentration. By increasing the $\omega_{PS\text{-}b\text{-}P4VP}$:$\omega_{FeCl3}$ ratio to 1:1, the hierarchical spherical pore structure is formed in the DMF solvent system, whereas the wormlike structure is formed in the 1,4-dioxane system, which signifies the initiation of the phase separation of the PS-b-P_4VP template in the sol-gel solution. The hierarchical structure in the DMF case can be assigned to the instability of the micellar structure, which leads to a partial fusion of the smaller spherical micelles. In addition, the distinctly different morphologies present in the DMF and 1,4-dioxane system can be attributed to the different preferential affinity of the solvent. Further increasing the $\omega_{PS\text{-}b\text{-}P4VP}$:$\omega_{FeCl3}$ ratio to 2:1 leads to the expansion of the spherical pore structure, whereas the wormlike pore structure shrinks. The expansion of the spherical pore structure can be explained by the increased average number of polymer chains in an aggregate (N_{agg}). However, the unique interconnected wormlike structure tends to deform into a more elongated wormlike structure for accommodating more polymer chains in the monolayer geometry. Moreover, DMF/1,4-dioxane solvent mixture with different component ratios are prepared for exploring the influence of the selectivity of the solvent on the nanostructure of the thin film. It is demonstrated that the spherical-to-wormlike porous structural transformation occurs at the critical $\Delta\chi$ value of 0.77 and the structural transformation leads to the expansion of the feature sizes of the nanostructures. The slight shrink of the feature size by increasing the volume fraction of 1,4-dioxane from 90 to 100 vol% is likely due to the viscosity difference between the DMF/1,4-dioxane cosolvent and the pure 1,4-dioxane. Except for the hybrid structure of the spherical and wormlike structure, the ordering of the nanostructures is gradually decreased with the increase of the 1,4-dioxane component in the cosolvent. Given by the advantages of large area homogeneity and multiple morphologies, the α-Fe_2O_3 thin films prepared in the present work show enormous application prospects in the fields of photovoltaics and sensors.

Supporting Information

Supporting Information is available from the Wiley Online Library or from the author.

Acknowledgements

This work was supported by funding from the Deutsche Forschungsgemeinschaft (DFG, German Research Foundation) under Germany's Excellence Strategy—EXC 2089/1—390776260 (e-conversion) and the International Research Training Group 2022 Alberta/Technical University of Munich International Graduate School for Environmentally

Responsible Functional Hybrid Materials (ATUMS), TUM.solar in the context of the Bavarian Collaborative Research Project Solar Technologies Go Hybrid (SolTech) and the Center for NanoScience (CeNS). S.Y., W.C., and N.L. acknowledge the financial support from China Scholarship Council (CSC). The authors thank Prof. Alexander Holleitner and Peter Weiser for providing access to the SEM. L.S. acknowledges the Natural Science Foundation of China (62004167) and the Joint Research Funds of the Department of Science & Technology of Shaanxi Province and Northwestern Polytechnical University (2020GXLH-Z-018). All GISAXS measurements were carried out at the light source PETRA III at DESY, a member of the Helmholtz Association (HGF).

Open access funding enabled and organized by Projekt DEAL.

Conflict of Interest

The authors declare no conflict of interest.

Data Availability Statement

The data that support the findings of this study are available from the corresponding author upon reasonable request.

Keywords

α-Fe_2O_3, GISAXS, PS-b-P_4VP, thin film morphology

Received: January 28, 2021
Revised: May 12, 2021
Published online:

[1] I. Barandiaran, G. Kortaberria, *RSC Adv.* **2015**, *5*, 95840.
[2] B. H. Sohn, J. M. Choi, S. I. Yoo, S. H. Yun, W. C. Zin, J. C. Jung, M. Kanehara, T. Hirata, T. Teranishi, *J. Am. Chem. Soc.* **2003**, *125*, 6368.
[3] H. G. Cha, J. Song, H. S. Kim, W. Shin, K. B. Yoon, Y. S. Kang, *Chem. Commun.* **2011**, *47*, 2441.
[4] S. Hou, P. Wang, Y. Li, F. Pang, M. Liu, Y. Luo, L. Zhuang, L. Zhao, *Appl. Surf. Sci.* **2019**, *476*, 959.
[5] C. G. Hardy, L. Ren, S. Ma, C. Tang, *Chem. Commun.* **2013**, *49*, 4373.
[6] X. Hu, J. C. Yu, J. Gong, Q. Li, G. Li, *Adv. Mater.* **2007**, *19*, 2324.
[7] D. Lei, M. Zhang, B. Qu, L. Chen, Y. Wang, E. Zhang, Z. Xu, Q. Li, T. Wang, *Nanoscale* **2012**, *4*, 3422.
[8] Z. Li, Y. Mao, Q. Tian, W. Zhang, L. Yang, *J. Alloys Compd.* **2019**, *784*, 125.
[9] Y. Liu, Y. X. Yu, W. D. Zhang, *Int. J. Hydrogen Energy* **2014**, *39*, 9105.
[10] A. M. Jubb, H. C. Allen, *ACS Appl. Mater. Interfaces* **2010**, *2*, 2804.
[11] Q. Luo, H. Chen, Y. Lin, H. Du, Q. Hou, F. Hao, N. Wang, Z. Guo, J. Huang, *Adv. Funct. Mater.* **2017**, *27*, 1702090.
[12] W. Hu, T. Liu, X. Yin, H. Liu, X. Zhao, S. Luo, Y. Guo, Z. Yao, J. Wang, N. Wang, H. Lin, Z. Guo, *J. Mater. Chem. A* **2017**, *5*, 1434.
[13] M. Shahpari, A. Behjat, M. Khajaminian, N. Torabi, *Sol. Energy* **2015**, *119*, 45.
[14] A. Manikandan, A. Saravanan, S. A. Antony, M. Bououdina, *J. Nanosci. Nanotechnol.* **2015**, *15*, 4358.
[15] Y. Jiang, D. Zhang, Y. Li, T. Yuan, N. Bahlawane, C. Liang, W. Sun, Y. Lu, M. Yan, *Nano Energy* **2014**, *4*, 23.
[16] T. Jiang, F. Bu, X. Feng, I. Shakir, G. Hao, Y. Xu, *ACS Nano* **2017**, *11*, 5140.
[17] S. Li, Y. Zhang, J. Huang, *J. Alloys Compd.* **2019**, *783*, 793.
[18] K. Fan, J. Guo, L. Cha, Q. Chen, J. Ma, *J. Alloys Compd.* **2017**, *698*, 336.
[19] S. S. Sangale, V. V. Jadhav, S. F. Shaikh, P. V. Shinde, B. G. Ghule, S. D. Raut, M. S. Tamboli, A. M. Al-Enizi, R. S. Mane, *Mater. Chem. Phys.* **2020**, *246*, 122799.
[20] S. H. Yun, B. H. Sohn, J. C. Jung, W. C. Zin, J. K. Lee, O. Song, *Langmuir* **2005**, *21*, 6548.
[21] Y. Yin, J. Zhao, L. Qin, Y. Yang, L. He, *RSC Adv.* **2016**, *6*, 63358.
[22] K. Wang, V. Körstgens, D. Yang, N. Hohn, S. V. Roth, P. Müller-Buschbaum, *J. Mater. Chem. A* **2018**, *6*, 4405.
[23] C. Zhang, J. Li, A. Belianinov, Z. Ma, C. K. Renshaw, R. M. Gelfand, *Nanotechnology* **2020**, *31*, 465302.
[24] T. Tamai, N. Ichinose, S. Kawanishi, M. Nishii, T. Sasuga, I. Hashida, K. Mizuno, *Chem. Mater.* **1997**, *9*, 2674.
[25] M. Domonkos, P. Demo, A. Kromka, *Crystals* **2020**, *10*, 118.
[26] Y. Mai, A. Eisenberg, *Chem. Soc. Rev.* **2012**, *41*, 5969.
[27] K. Wang, S. Xia, W. Cao, N. Hohn, S. Grott, L. P. Kreuzer, M. Schwartzkopf, S. V. Roth, P. Müller-Buschbaum, *ACS Appl. Nano Mater.* **2018**, *1*, 7139.
[28] S. Park, B. Kim, O. Yavuzcetin, M. T. Tuominen, T. P. Russell, *ACS Nano* **2008**, *2*, 1363.
[29] J. P. Spatz, S. Mössmer, C. Hartmann, M. Möller, T. Herzog, M. Krieger, H. G. Boyen, P. Ziemann, B. Kabius, *Langmuir* **2000**, *16*, 407.
[30] A. Rahikkala, A. J. Soininen, J. Ruokolainen, R. Mezzenga, J. Raula, E. I. Kauppinen, *Soft Matter* **2013**, *9*, 1492.
[31] M. M. Abul Kashem, J. Perlich, L. Schulz, S. V. Roth, W. Petry, P. Müller-Buschbaum, *Macromolecules* **2007**, *40*, 5075.
[32] Y. Yao, E. Metwalli, M. A. Niedermeier, M. Opel, C. Lin, J. Ning, J. Perlich, S. V. Roth, P. Müller-Buschbaum, *ACS Appl. Mater. Interfaces* **2014**, *6*, 5244.
[33] S. Zou, R. Hong, T. Emrick, G. C. Walker, *Langmuir* **2007**, *23*, 1612.
[34] S. Yin, T. Tian, K. S. Wienhold, C. L. Weindl, R. Guo, M. Schwartzkopf, S. V. Roth, P. Müller-Buschbaum, *Adv. Mater. Interfaces* **2020**, *7*, 2001002.
[35] S. Yin, L. Song, S. Xia, Y. Cheng, N. Hohn, W. Chen, K. Wang, W. Cao, S. Hou, P. Müller-Buschbaum, *Small Methods* **2020**, *4*, 1900689.
[36] L. Zhang, A. Eisenberg, *Polym. Adv. Technol.* **1998**, *9*, 677.
[37] L. Zhang, K. Yu, A. Eisenberg, *Science* **1996**, *272*, 1777.
[38] Y. Chen, W. Zhao, J. Zhang, *RSC Adv.* **2017**, *7*, 4226.
[39] A. Buffet, A. Rothkirch, R. Döhrmann, V. Körstgens, M. M. Abul Kashem, J. Perlich, G. Herzog, M. Schwartzkopf, R. Gehrke, P. Müller-Buschbaum, S. V. Roth, *J. Synchrotron Radiat.* **2012**, *19*, 647.
[40] G. Benecke, W. Wagermaier, C. Li, M. Schwartzkopf, G. Flucke, R. Hoerth, I. Zizak, M. Burghammer, E. Metwalli, P. Müller-Buschbaum, M. Trebbin, S. Förster, O. Paris, S. V. Roth, P. Fratzl, *J. Appl. Crystallogr.* **2014**, *47*, 1797.
[41] T. Ahmad, A. Ganguly, J. Ahmed, A. K. Ganguli, O. A. A. Alhartomy, *Arabian J. Chem.* **2011**, *4*, 125.
[42] L. Wang, X. Lu, C. Han, R. Lu, S. Yang, X. Song, *CrystEngComm* **2014**, *16*, 10618.
[43] Y. Yan, H. Tang, F. Wu, R. Wang, M. Pan, *Energies* **2017**, *10*, 1296.
[44] X. F. Lu, X. Y. Chen, W. Zhou, Y. X. Tong, G. R. Li, *ACS Appl. Mater. Interfaces* **2015**, *7*, 14843.
[45] L. Zhang, H. Shen, A. Eisenberg, *Macromolecules* **1997**, *30*, 1001.
[46] S. R. Bakaul, W. Lin, T. Wu, *Appl. Phys. Lett.* **2011**, *99*, 042503.
[47] B. Ziberi, F. Frost, T. Höche, B. Rauschenbach, *Phys. Rev. B* **2005**, *72*, 235310.
[48] K. Wang, L. Biessmann, M. Schwartzkopf, S. V. Roth, P. Müller-Buschbaum, *ACS Appl. Mater. Interfaces* **2018**, *10*, 20569.
[49] S. Park, D. H. Lee, J. Xu, B. Kim, S. W. Hong, U. Jeong, T. Xu, T. P. Russell, *Science* **2009**, *323*, 1030.
[50] N. Hohn, S. J. Schlosser, L. Biessmann, S. Grott, S. Xia, K. Wang, M. Schwartzkopf, S. V. Roth, P. Müller-Buschbaum, *Nanoscale* **2018**, *10*, 5325.
[51] R. Hosemann, S. N. Bagchi, *Acta Crystallogr.* **1952**, *5*, 612.
[52] G. Santoro, A. Buffet, R. Döhrmann, S. Yu, V. Körstgens, P. Müller-Buschbaum, U. Gedde, M. Hedenqvist, S. V. Roth, *Rev. Sci. Instrum.* **2014**, *85*, 043901.
[53] S. O'Driscoll, G. Demirel, R. A. Farrell, T. G. Fitzgerald, C. O'Mahony, J. D. Holmes, M. A. Morris, *Polym. Adv. Technol.* **2011**, *22*, 915.
[54] Y. Yu, L. Zhang, A. Eisenberg, *Macromolecules* **1998**, *31*, 1144.
[55] B. Jiang, B. Wang, L. Zhang, Y. Sun, X. Xiao, N. Yang, H. Dou, *Sep. Sci. Technol.* **2016**, *51*, 2940.